Title

Backscatter tensor imaging and 3D speckle tracking for simultaneous ex vivo structure and deformation measurement of myocardium.

Journal

Ultrasound in Medicine and Biology, 49(5)

Authors

Cormack, John
Simon, Marc
Kim, Kang

Publication Date

2023-05-01

DOI

10.1016/j.ultrasmedbio.2023.01.009

Peer reviewed

HHS Public Access

Author manuscript

Ultrasound Med Biol. Author manuscript; available in PMC 2024 May 01.

Published in final edited form as:

Ultrasound Med Biol. 2023 May ; 49(5): 1238–1247. doi:10.1016/j.ultrasmedbio.2023.01.009.

Backscatter tensor imaging and 3D speckle tracking for simultaneous ex vivo structure and deformation measurement of myocardium

John M. Cormack[a,b,*], **Marc A. Simon**[c], **Kang Kim**[a,b,d]

[a]Center for Ultrasound Molecular Imaging and Therapeutics, University of Pittsburgh Medical Center, Pittsburgh, Pennsylvania 15261-1909, USA

[b]Division of Cardiology, Department of Medicine, University of Pittsburgh, Pittsburgh, Pennsylvania 15261, USA

[c]Division of Cardiology, Department of Medicine, University of San Francisco Medical Center, San Francisco, California 94117, USA.

[d]Department of Bioengineering, University of Pittsburgh, Pittsburgh, Pennsylvania, 15213, USA.

Abstract

Objective: Biaxial mechanical testing is a common method for elucidation of mechanical properties of excised ventricular myocardium, especially in the context of structural remodeling that accompanies heart disease. Current imaging strategies in biaxial testing are based on optical camera imaging of the tissue surface, thus providing no information about the tissue microstructure and limiting strain measurements to two dimensions. Here, these limitations are overcome by replacing the camera with ultrasound imaging in order to measure both transmural fiber orientation and 3D tissue deformation during biaxial testing.

Methods: Quasi-static biaxial mechanical testing is applied to four samples of excised porcine ventricular myocardium (two left- and two right-ventricular tissues). During testing, a rotational scan of an ultrasound linear array provides data for both backscatter tensor imaging and 3D speckle tracking, from which transmural fiber orientation and tissue deformation are computed, respectively. Ultrasound-derived fiber orientation and tissue strain are validated against histology and camera surface imaging, respectively.

Discussion: Ultrasound-derived fiber angle and tissue strain exhibit good accuracy, with root-mean-square errors of 9.9° and 1.2% strain, respectively. Further investigation into the optimization of backscatter tensor imaging is warranted. Replacing the rotational scan of a linear array with volume imaging with a matrix array will improve the technique.

[*]Corresponding Author: John M. Cormack, 3550 Terrace Street, Pittsburgh, PA 15261; jmc345@pitt.edu; Phone, (412) 624-2264.

Conflicts of Interest

The authors have no conflicts of interest to report.

Conclusion: Ultrasound imaging can replace the optical camera measurement during biaxial mechanical testing of ventricular myocardium in order to accurately provide measurements of transmural fiber orientation and tissue strain. In situ knowledge of transmural fiber structure and tissue deformation can enhance the inverse problem used to determine tissue mechanical properties from biaxial testing.

Keywords

Backscatter tensor imaging; 3D speckle tracking; Biaxial mechanical testing; Ventricular myocardium; Pulmonary hypertension

1. Introduction

Ventricular myocardium is composed of laminar sheets of myofibers and collagen that exhibit smoothly varying orientation between the outer (epicardium) and inner (endocardium) surfaces.[1] The helical transmural variation of fiber orientation controls the mechanical and electrical behavior of the ventricles,[2] and is known to be altered in diseased states such as in the left ventricle (LV) after infarction[3] and in the right ventricle (RV) during chronic pulmonary hypertension,[4] as well as during natural healthy aging.[5] Ventricular myocardium is mechanically anisotropic and hyperelastic due to the fibrous and layered structure of myocardium.[4] Experimental investigation of the fiber structure and mechanical properties of ventricular myocardium is a wide-reaching field of research, including evaluation of the mechanical effects of therapeutic drugs[6] and determination of mechanical properties for use in detailed whole-heart finite element models.[7]

The current standard method for mechanical experimentation of passive myocardium is biaxial mechanical testing (BMT) of excised ventricular tissue. BMT enables determination of the tissue anisotropic and hyperelastic stiffness proprieties by applying independent tissue loading along two orthogonal axes. The force required to deform the tissue is measured with load cells in line with the BMT actuators, and the tissue deformation is measured usually by tracking superficial markers in optical camera images of the tissue surface. Fiber structure is determined post hoc with destructive histological sectioning. The two-dimensional stress and strain measurements obtained during BMT are coupled with the transmural fiber orientations obtained from histology, along with assumptions of plane stress and incompressibility, during solution of the inverse problem to determine the tissue mechanical properties.

Thus the major limitations of the current state of the art are with the optical camera strain measurement, in particular the inability to measure out of plane deformation, transmural variation of deformation, and the transmural fiber microstructure during mechanical testing. These limitations are most obvious for thick samples for which the plane stress assumption may be invalid; for example, human left ventricular myocardium, which is around 13–15 mm in full thickness, must be thinned to reduced thicknesses in order to perform BMT with current methods.[7] Previous studies have employed translational scanning of an ultrasound linear imaging array to measure the three-dimensional transmural deformation with 3D ultrasound speckle tracking (3DUST), and used the subsequent 2D stress and 3D strain data

to infer the transmural fiber orientation by optimizing a constitutive model to match the measurements.[8,9]

Recently, Papadacci et al.[10] introduced ultrasound backscatter tensor imaging (BTI) in which the transmural fiber orientation of excised porcine LV myocardium was estimated using a rotational scan of a linear imaging array by measuring the direction dependence of the spatial coherence of ultrasound echoes. The spatial coherence of echoes is proportional to the alignment of the ultrasound array with the microstructure in the focal region.[11] The technique was later used in open chest sheep and *in vivo* human experiments with a 2D matrix ultrasound imaging array,[12] and more recently used in simulations to estimate the fiber directional strain in a finite element model of a beating left ventricle.[13]

In the present work, a new experimental configuration is introduced that employs a rotational scan of an ultrasound linear array during quasi static BMT of excised left- and right-ventricular porcine myocardium. From the rotational ultrasound scan, the fiber orientation is estimated using BTI and the three dimensional tissue deformation is computed using 3DUST. The ultrasound-based fiber orientation and tissue strain measurements are validated against destructive histology and optical measurement of surface strains, respectively. The new experimental configuration improves upon current methods for BMT by enabling simultaneous measurement of fiber structure along with three dimensional tissue deformation throughout the tissue volume.

2. Methods

2.1. Tissue Specimen Preparation

Fresh-frozen porcine hearts were obtained from a local grocery store and thawed in a refrigerator prior to excision of the tissue samples. Square tissue samples with approximate dimensions of 20×20×5 mm were excised from the left- and right-ventricular free walls in the locations approximately identified in Fig. 1. Two LV and two RV samples were used in this study. Fullthickness tissues (~20 mm for LV and ~10 mm for RV tissues) are too thick for biaxial testing, so samples were thinned to approximately 5 mm thickness [Fig. 1(B) and (D)]: the final LV samples were mid-wall myocardium, i.e., both epicardium and endocardium were removed; the RV sample comprised the epicardium and myocardium, i.e., only trabeculation of the endocardium was removed prior to testing.

2.2. Biaxial Mechanical Testing and Ultrasound Scanning

A schematic of the experimental configuration employed in this work is depicted in Fig. 2(A). The square tissue sample is loaded into a biaxial mechanical testing (BMT) machine (BioTester, CellScale, Waterloo, ON, Canada) using sutures and fish hooks in order to minimize shear loading and torques.[14,15] Directions of the BMT actuator motion correspond to X and Y directions of the Cartesian coordinate frame employed here [Fig. 2(B)]. The sample is submerged in de-gassed Phosphate Buffered Saline (PBS) throughout testing, the temperature of which was near room temperature at 27°C. A small preload of approximately 75 mN in both directions is initially applied while maintaining the square aspect ratio of the

sample. Two-protocol biaxial stretching was employed, in which the actuator displacements in the two loading protocols have ratios of 1:1 and 1:2 (X:Y), respectively.[8,9]

Prior to testing, each sample was preconditioned by stretching to the maximum equibiaxial strain for 5 cycles. The actuator displacement in both X and Y directions is 5 mm for these cycles. Each cycle consists of stretch at 0.17 mm/s (quasi static), holding in the stretched configuration for 82 s, relaxation at the same rate, and holding there for 82 s. During these preconditioning cycles, significant damage to the tissue occurs,[15] leading to sagging of the sample in the unstretched configuration. To account for this non-elastic deformation and eliminate the sagging, which confounds ultrasound imaging, the sample is re-preloaded to near 75 mN by increasing the reference size by approximately 1 mm in each direction. Biaxial testing of the sample then consists of 3 additional preconditioning cycles to the same maximum equibiaxial stretch as the first preconditioning cycles (i.e., approximately 4 mm from the new reference configuration), followed by the two-protocol testing. During two-protocol testing, the sample was stretched to increasingly higher strain, alternating loading protocols at each level of stretch. Six levels of stretch were employed for each, yielding 12 total deformed configurations. Forces required to apply the deformations were measured with 23 N-capacity load cells (CellScale) at a sampling rate of 5 Hz.

A rotational ultrasound imaging scan was performed in the reference configuration (after re-preloading) and at each of the 12 deformed configurations while the sample is held stationary. The ultrasound probe is a 128-element linear array with center frequency 18 MHz, pitch of 0.1 mm, and elevational focus at 8 mm (L22–14v, Verasonics, Kirkland, WA, USA). Ultrasound imaging acquisitions and scanning of the motorized rotational stage (Velmex, Rochester, NY, USA) are controlled with a programmable ultrasound platform (Vantage 128, Verasonics). Prior to testing, the rotation axis of the rotational stage was closely aligned with the ultrasound array imaging axis by imaging a 1/4” (6.35 mm) diameter ball bearing; misalignment was negligible axially (Z) and a maximum of 100 μm laterally (X or Y). Ultrasound acquisitions are based on those of Ref. 10: Each image was obtained using coherent plane wave compounding with 41 plane waves with tilt angles that range from −20° to 20° in steps of 1°. The rotational scan consists of 72 such images acquired over 360° in steps of 5°, which takes place over about 79 s while the sample was held in each stretched configuration. No creep or change in deformation was observed during the ultrasound scan while the sample is held stretched, although noticeable creep occurs in each cycle after the load is removed.

2.3. Ultrasound Myofiber Imaging

The transmural fiber orientation in the reference configuration and each of the deformed configurations was determined using backscatter tensor imaging (BTI) based on the procedure described by Papadacci et al.[10] Briefly, BTI employs a rotational scan of a linear array to identify the orientation at which the spatial coherence of the backscattered RF echoes is greatest. The spatial coherence is proportional to the autocorrelation length of the microstructure in the ultrasound focal region in the direction of the ultrasound array (u direction in Fig. 3),[11] thus the direction of maximum spatial coherence corresponds to the fiber direction and the minimum spatial coherence is perpendicular to that direction (Fig.

3). Plane wave compounding enables the synthesis of a focus in transmit and receive at any point, thus the coherence can be computed anywhere in the imaging region using fewer transmit events compared to conventional focused-wave imaging.

Ultrasound image formation and spatial coherence calculation for BTI analysis was performed with a modified coherent plane wave compounding routine that accounts for the slower sound speed in the PBS compared to the sound speed in the myocardium.[16] Sound speeds were assumed to be equal to 1480 m/s and 1540 m/s for the PBS and myocardium, respectively, based on pilot measurements. Spatial coherence of the RF data was quantified by the coherence factor[10,17]

$$C = \frac{\sum_{T_1}^{T_2} \left| \sum_{k=1}^{N} s(u_k, t) \right|^2}{N \sum_{T_1}^{T_2} \sum_{k=1}^{N} \left| s(u_k, t) \right|^2}, \tag{1}$$

where $s(u_k,t)$ is the time-delayed and compounded RF signal corresponding to the k^{th} element of the receive aperture (i.e., before summation over the receive aperture takes place), N is the number of elements in the receive aperture, and the range $T_1 < t < T_2$ defines a temporal window centered at the focal time ($T_2 - T_1 \approx 0.19\ \mu s$, or 3.5 cycles at the RF center frequency, in this work). The coherence factor takes a value in the range $0 < C < 1$, where $C = 0$ corresponds to no spatial coherence of the received echo over the receive aperture, and $C = 1$ corresponds to total coherence, i.e., the beamformed wavefront arrives simultaneously at all points along the receive aperture. Total coherence $C = 1$ occurs for perfect beamforming of the echo from an ideal point target.

For each B mode image taken with the linear array at angle θ, the coherence factor C is computed from RF data at each pixel in a 3 mm wide region centered on the imaging axis $u = 0$, which corresponds to the probe rotation axis during the scan. Variation of coherence within the imaging region is associated not only with the fiber microstructure, but also may be caused by coherent scattering from echogenic tissue inhomogeneities that are not associated with the fibers. To account for these inhomogeneities, an axial moving average of C is performed at each Z by computing the mean of all values within a kernel centered at $u = 0$ and Z with dimensions 3 mm in width and 0.25 mm axially in order to obtain the variation of C with Z for each probe orientation θ. Thus the function $C(\theta, Z)$ is determined from the rotational scan in each deformed configuration. Maxima and minima in C occur when the array is oriented along and across the fibers, respectively, thus the fiber angle at each depth is determined from a cosine fit to $C(\theta, Z)$ at each Z with period of 180°:

$$C(\theta, Z) \approx A_0(Z) + A_1(Z) \cos[2(\theta - \theta_{\text{fib}})], \tag{2}$$

where $A_0(Z)$ is the mean coherence, $A_1(Z)$ corresponds to the modulation of coherence due to the fiber microstructure, and $\theta_{\text{fib}}(Z)$ is the fiber angle. In Eq. (2) the angles θ and θ_{fib} have units of radians. Directional variation of the backscatter coherence is quantified by the fractional anisotropy,

$$\text{FA} = \frac{A_1}{\sqrt{(A_0^2 + A_1^2)/2}}, \tag{3}$$

where FA = 0 indicates isotropy.

2.4. Three-dimensional Displacement and Strain Estimation

The displacement field in the tissue in each configuration is also determined from the rotational ultrasound scan. For use in 3DUST, each 2D image in the rotational scan is formed by assuming a constant sound speed of 1510 m/s in the imaging region (equal to the average of the assumed sound speeds in the PBS and myocardium). Whereas beamforming is accomplished with a two-layer refraction-corrected approach for BTI calculations, jitter on the order of 100 μm associated with estimation of the depth of the fluid-tissue interface in each deformed configuration eliminates consistency between reference frames that is needed for strain calculation from the displacement fields obtained from 3DUST. Therefore images for use in 3DUST are obtained by assuming a constant sound speed in the imaging region so that the reference frames for displacement estimation are consistent between deformed configurations, thus ensuring accuracy of the strain calculation.

A 3D B mode image is formed from the 2D images obtained at each θ by mapping the brightness values to a Cartesian X, Y, Z grid from the cylindrical coordinates of the rotational scan. The Cartesian coordinates are defined so that X corresponds to $\theta = 0$ and Z to the ultrasound imaging axis. The Cartesian grid had a spacing of 48 μm in the axial Z direction and 100 μm in the lateral X and elevational Y directions.

Displacements for each loading protocol are calculated using speckle tracking based on 3D normalized cross correlation[18] of 3D B mode images of consecutive deformed configurations. Speckle tracking was performed for each pair of 3D B mode images in 13 equally spaced Y-Z planes between $X = \pm 3$ mm. The cubic kernels for speckle tracking varied in size for each calculation in order to obtain tracking with high correlation throughout the tissue volume. Kernel volume edge sizes ranges from 0.5 to 1.2 mm, with larger sizes generally required to track larger displacements in order to account for the natural loss of speckle coherence that is proportional to displacement. Small kernels may be employed to track smaller displacements to save computation time when possible. Displacements of up to 1.2 mm are able to be tracked in this way.

Based on their coordinates $\mathbf{X} = [X, Y, Z]^T$ in the reference configuration, the trajectories $\mathbf{x}(\mathbf{X})$ of particles are found by accumulating the computed displacements throughout the deformation for each protocol. For each location in the tissue reference configuration $\mathbf{X}$, the position in the subsequent deformed configuration is obtained from $\mathbf{x} = \mathbf{X} + \mathbf{u}$, where $\mathbf{u}$ is determined from 3DUST. The trajectory of a given point $\mathbf{X}$ through the deformation for each loading protocol is accumulated in this way, where interpolation is used to estimate $\mathbf{u}$ if the position $\mathbf{x}$ does not fall onto the grid on which 3DUST was performed. Displacement accumulation is performed for all well-tracked and tissue-bound pixels, where ‘well-tracked’ and ‘tissue-bound’ are defined for each loading protocol by 3DUST correlation greater than 0.7 and B mode brightness greater than −50 dB, respectively, for each calculation throughout the loading protocol.

The deformation is quantified by

$$\mathbf{F} = \mathbf{I} + \frac{\partial \mathbf{u}}{\partial \mathbf{X}}, \tag{4}$$

$$\mathbf{E} = \frac{1}{2}(\mathbf{F}^T\mathbf{F} - \mathbf{I}), \tag{5}$$

where **F** and **E** are the deformation gradient and Lagrange (Green) strain tensors, and **I** is the identity tensor. The gradients in Eq. (4) are computed by fitting a linear model to tissue particle locations, i.e., $x_i \approx \text{const.} + F_{i1}X + F_{i2}Y + F_{i3}Z$, in the least-squares sense to well-tracked points within a sphere of radius D centered on **X**. The distance was set to D = 2 mm for this work. Note that calculated locations in the trajectories **x**(**X**) need not fall on a regular grid for strain calculation.

2.5. Validation

2.5.1. Fiber orientation validation with histology—Transmural fiber angle variation derived from BTI is validated against the ground truth of optical microscopy after histological sectioning. Samples were fixed immediately after testing in 10% neutral buffered formalin, then sectioned and stained with H&E. Digital images of each section are taken with a trinocular microscope [Fig. 4(A), 1.08 μm/pixel, field of view 2.76 mm × 2.08 mm], and the fiber angle determined with the OrientationJ/DistributionJ toolbox[19] in ImageJ (imagej.nij.gov) with local window set to 40 pixels (43.2 μm), minimum coherency to 2%, and minimum energy to 2%. Similar to previous studies,[4,6] the fiber angle and dispersion are reported as the circular mean and circular standard deviation, respectively, of the computed pixel-level local orientations. Fiber angle as computed with histology is compared to that obtained using BTI in the reference configuration.

In the comparison for each sample, rigid rotation of the sample was allowed for between the *in situ* configuration during biaxial testing and the orientation of each section as glued to the microscope slide by adding or subtracting a uniform value to each histology-derived fiber angle that minimizes the RMS difference between the two measurements. This enables compensation for rigid rotations resulting from misalignment of the sample edges with the X and Y directions during ultrasound scanning, which can occur do to the shear-minimizing pulley attachments employed during BMT.[14] Other discrepancies between the ultrasound measurement and histology, such as viscoelastic relaxation after removal from the BMT machine or distortions during fixation in formalin and embedding in paraffin prior to sectioning, are not able to be accounted for in this study.

2.5.2. Strain validation with optical camera—After the dual loading protocol was executed with ultrasound rotational scans obtained at each deformed configuration, the ultrasound array was removed and a CCD camera put in place to image the surface of the sample. The camera field of view was carefully aligned with the center of the sample, approximating the center of deformation during stretch [Fig. 4(B), 8.5 μm resolution, 8.1 × 10.8 mm field of view]. The three preconditioning cycles and 12 dual loading protocol cycles were repeated, with images obtained of the tissue surface at a rate of 1 Hz. The assumption of repeatability of the tissue deformation was validated previously

by performing back-to-back measurements, both times using the camera to measure tissue strain (data not shown).

Tissue surface strain was computed from the camera images by comparing images in each deformed configuration with the reference configuration. No visual tracking markers or other optical contrast were used as it was found that these interfered with the ultrasound measurement. The natural texture of the fibrous tissue was sufficient for correlation-based tracking of the camera images. Nine clusters of about ten points each were tracked to simulate tracking of visual tracking markers.[15] Quasirandom clusters of tracking points were preferred over a regular grid of tracking points in this work both in order to mimic the tracking strategy of Sommer et al.,[7] and also because it was found that strain estimation using the present strategy is more robust to the small-scale heterogeneity of surface displacement that results from relative fiber motion. Tracking calculations in optical images were performed using the LabJoy software (CellScale). Two-dimensional displacements and strains at the tissue surface are calculated as described in Sec. 2.4 by determining values in **F** by fitting a linear model to the computed particle trajectories based on their initial position for each loading protocol.

Surface strains can not be obtained from 3DUST,[8,9] but instead strains very near the tissue surface may be compared to those computed from camera images. Normal (E_{XX} and E_{YY}) and shear (E_{XY}) tissue strains computed using 3DUST are averaged over a disk with thickness 0.25 mm and diameter 4 mm located approximately 0.5 mm below the tissue surface, as identified in the B mode image, for comparison with those computed using camera images.

3. Results

3.1. Ultrasound Myofiber Imaging

Examples of backscatter coherence variation versus imaging array orientation (probe angle) and tissue thickness are presented in Figs. 5(A) and (C) for one LV and one RV specimen, respectively. The coherence is presented as normalized by the mean at each depth $A_0(Z)$. For each tissue there are apparent bands of alternating low (blue) and high (red) coherence spaced by approximately 90°, indicating sensitivity of the backscatter coherence to the fibrous microstructure of the tissue. At each depth the orientation of the array with maximum coherence corresponds to the fiber direction, and minimum coherence is the direction perpendicular to the fiber direction. In both Figs. 5(A) and (C) it is apparent that the contrast in coherence between the across- and along-fiber directions increases with imaging depth. This may be due to isotropic interference caused by strong reflections at the fluid-tissue interface, which results in decreased anisotropy of C close to the interface near to the imaging array. Similar reduced performance of BTI was attributed to these effects in a simulation experiment of BTI.[20] Another possible cause could be that the elevational focal depth of the imaging array at 8 mm is closer to the lower surface of the tissue [approximately 10 mm and 9 mm in Figs. 5(A) and (C), respectively, whereas the upper surface depth is approximately 3 mm for both samples], thus providing superior ultrasound focusing in transmit at those depths.

The fiber direction is determined from the cosine fit, Eq. (2), examples of which are shown in Figs. 5(B) and (D) corresponding to the coherence at 50% thickness through each tissue sample. In each case the cosine fit is good with $R^2 \approx 0.85$, further indicating that variation of the coherence with probe angle is sensitive to the orientation of the myofibers. In Fig. 5(C) the 180° periodicity is lost after about 80% thickness, which approximately corresponds to the beginning of the epicardial layer [the epicardium corresponds to 100% thickness in Fig. 5(C)]. The rapid variation in tissue microstructure in that region of tissue thickness, which is unique to porcine RV myocardium,[21] confounds BTI and renders estimation of the fiber orientation there infeasible.

Accuracy of BTI for estimation of the fiber angle is demonstrated in Fig. 6. The fiber angle predicted by ultrasound with BTI is compared to that obtained from microscopy analysis of histological sections in Figs. 6(A) and (B) for the same LV and RV samples that appear in Fig. 5. Error bars for ultrasound represent uncertainty in the least-squares fit of Eq. (2) at each depth, and those for histology represent pixel orientation dispersion computed with OrientationJ. Good agreement is observed throughout the thickness in each case, apart from the epicardial layer that is indicated in Fig. 6(B) by the gray box. In that region the rapid variation of microstructure is evidenced by the jump in fiber angle from −30° though more than 90° to approximately 45° in less than 500 μm of tissue thickness. A histogram of error, defined as the difference between ultrasound- and histology-derived fiber angle, is presented in Fig. 6(C) for all data from the four samples tested (excluding the epicardial layer of RV tissues). The root-mean-square error (RMSE) of BTI, taking histology as the ground truth, is 9.9° in this study, comparable to previously reported comparisons in porcine LV myocardium.[12] Angles of rigid rotation across the four samples required to align histology with the ultrasound-derived transmural fiber variation were 6.9 ± 6.0°.

Transmural variation of coherence fit parameters is presented in Fig. 7. In each panel the metrics from each individual sample are represented by black dashed curves, and the mean across samples at each depth by blue solid curves. In each panel the overall average of each metric $\langle \cdot \rangle$ is presented, with the variation represented by the overall standard deviation. Again data from the epicardial regions of RV samples has been excluded. The average coherence A_0 [Fig. 7(A)] decreases slightly with depth, likely due to increasing error in beamforming with increasing distance from the imaging array. Coherence modulation amplitude A_1 [Fig. 7(B)] remains fairly constant transmurally, and the fractional anisotropy [Eq. (3), Fig. 7(C)] increases with depth due to the decrease of A_0. The increase in fractional anisotropy possibly results from isotropic interface effects discussed in connection with Fig. 5.

The overall average values for the coherence metrics reported in Fig. 7, which are consistent with our previous work,[16] may be compared to those reported by Papadacci et al.[10] where BTI is performed on porcine LV myocardium embedded in gelatin using ultrasound imaging at 6 MHz. There they report $\langle A_0 \rangle \approx 0.5$, $\langle A_1 \rangle \approx 0.2$, and $\langle \mathrm{FA} \rangle \approx 0.42$, all considerably higher than the values reported in Fig. 7 for the present study. The differences could be due to the higher imaging frequency employed in this study, which is more susceptible to degraded coherence due to scattering from off-axis inhomogeneities that are not related to the fiber structure. Another possible factor is load dependence of backscatter coherence and

its anisotropy, which can be influenced by residual stresses in the ventricular free wall that can differ between individual animals and hearts depending on the organ preparation and tissue sample excision.

3.2. 3D Strain Estimation

Here 3DUST results are reported for only three of the four tested samples; validation with optical camera measurement for one RV sample failed due to significant misalignment of the camera and ultrasound fields of view. Tri-plane depictions of the 3D ultrasound B mode image, the three components of displacement calculated using 3DUST, and the six component of the strain tensor are presented in Fig. 8 for the other RV sample. The boundary of the epicardial layer is clearly visible at approximately $Z = 11$ mm in the B mode image [Fig. 8(A)], but otherwise the speckle pattern is uniform. The displacements and strains correspond to the configuration of greatest deformation in loading protocol #1 (approximately equibiaxial). Both u_X and u_Y displacement fields exhibit a small amount of nonuniformity through the tissue volume. Variation of u_Y with X is apparent, corresponding to in-plane shear deformation. The axial displacement u_Z is negative throughout the volume due to average motion of the sample towards the imaging array during the applied loading as the sample becomes more taught under increasing tension. The gradient in u_Z with Z results from Poisson's effect due to the low compressibility of the tissue sample.

Variation in 3D of the six components of the strain tensor **E** is also illustrated in Fig. 8. Most of the deformation is accounted for by the normal strain components in Figs. 8(E)–(G). While there is significant in-plane shear stain E_{XY} [Fig. 8(H)], out-of-plane shear is much smaller in magnitude [Figs. 8(I) and (J)].

Accuracy of 3DUST to determine the strain experienced by the sample is presented in Fig. 9. Direct comparison of the strains at the sample surface calculated using 3DUST and using the CCD camera images (ground truth) are shown in Figs. 9(A) and (B) for loading protocols #1 and #2, respectively, for the same RV sample depicted in Fig. 8. Good agreement is observed at all deformed configurations in each of the three components of surface strain, including both normal [E_{XX} (blue curves) and E_{YY} (red curves)] and shear [E_{XY} (green curves)] components. A Bland-Altman plot is presented in Fig. 9(C) of all comparisons between 3DUST and camera measurements of surface strain. The RMSE of 3DUST compared to that measured by CCD camera is equal to 0.012 strain, comparable with previous studies by our group using a lateral ultrasound scan with higher imaging frequency (30 MHz) to generate 3D B mode images of excised rat LV myocardium under biaxial tension.[9]

With the strain field calculated from 3DUST and known throughout the tissue volume, some common assumptions in BMT experiments may be examined. One such assumption is that of plane stress, in which it is assumed that no stress may occur in the Z direction, and that both stress and strain have no variation in Z. Variation of normal strain components through the tissue sample thickness for three samples is shown in Fig. 10, along with percent variation through the tissue thickness (defined for each component as transmural standard deviation normalized by the transmural mean). Slight variation is apparent in each normal strain component for each sample, with mean across the nine measurements of 7.2 ±

3.0%. The transmural variation observed in this study could be due in part to physiological transmural variation in the tissue structure and mechanical properties, and also could in part be due to the precise loading condition enacted on the tissue edges by the fish hooks that attach the sample to the actuators.

Another common assumption employed in BMT of tissues is that of tissue incompressibility. An incompressible material must exhibit no local volume change, which is represented mathematically by the condition $\det \mathbf{F} = 1$. This condition may be evaluated for the samples tested here, as the deformation tensor $\mathbf{F}$ is calculated throughout the tissue volume according to Eq. (4) using the displacement fields obtained from 3DUST. In Fig. 11, the mean transmural value of $\det \mathbf{F}$ versus mean principle tensile strain $E_{1,2}$ (mean of the positive eigenvalues of the strain tensor) for each deformed configuration of loading protocol #1 for each sample is presented. The magnitude of volume change (10–20%) and the small sample size employed in this study preclude definitive conclusion of the validity of the incompressibility assumption. However, similar magnitudes of volume changes as reported in Fig. 11 were recently reported in excised porcine and human ventricular myocardium in recent simulations of BMT based on direct measurements of tissue compressiblity in excised samples.[22] *In vivo* measurements of ventricular compressibility suggest that compressibility may be accounted for to enhance patient-specific whole-heart modeling efforts.[23] Transmural strain estimation with 3DUST may be employed in order to account for tissue compressiblity in future biaxial testing experiments.

Finally, a representative stress-strain curve corresponding to loading protocol #1 (approximately equibiaxial) is presented for an RV tissue sample in Fig. 12, where normal components of the second Piola-Kirchhoff (PK) tensor $\mathbf{S}$ are plotted versus mean principle tensile strain $E_{1,2}$. The second PK stress $\mathbf{S} = \mathbf{P}\mathbf{F}^{-1}$, where $\mathbf{P}$ is the first Piola-Kirchhoff tensor, is computed from biaxial load cell data using the formulation given by Sommer et al.[15] The curves indicate that the RV tissue sample exhibits anisotropy and hyperelasticity typical of ventricular myocardium. The mean fiber angle for this sample is −18° relative to the X axis, so that the X and Y directions correspond approximately to along- and across-fiber directions, respectively. Magnitudes of the stress are similar to those reported previously in biaxial mechanical experiments on passive porcine RV myocardium.[24]

4. Summary and discussion

A new experimental configuration is presented that combines ultrasound imaging and biaxial mechanical testing of excised myocardium to gain both transmural structural and mechanical tissue information during testing. Structural information is obtained with backscatter tensor imaging using a rotational scan of an ultrasound linear array, from which the transmural variation of the fiber orientation is determined from the direction dependence of ultrasound spatial coherence. Ultrasound B mode images from the rotational scan are also used to obtain 3D B mode images, from which the 3D tissue deformation is calculated using 3D ultrasound speckle tracking with normalized cross correlation. The ultrasound-derived fiber orientation and tissue strain are validated against ground truths of histology and CCD camera measurements of the surface deformation, respectively. The new experimental configuration thus overcomes the major limitations of current practice in biaxial mechanical

testing, in which no structural information is obtained *in situ* and only 2D measurements of surface deformation are found with optical measurement of the sample surface. Compared to current practice, the new ultrasound-based measurement thus provides *in situ* knowledge of the fiber orientation and 3D tissue strain, including out of plane deformations.

Further investigation of the fiber and strain imaging modalities is warranted. Investigations into the origins of discrepancies in BTI readouts between the present study and Papadacci et al.[10] that are discussed in Sec. 3 in connection with Figs. 6 and 7 may shed invaluable light on how imaging parameters (e.g., frequency and imaging depth) and tissue microstructure (e.g., dispersion of fiber angles in a given sheet and residual stress) affect the performance of BTI. Finer details of discrepancies between fiber angle predicted by BTI and histology, such as those near 30% thickness in Fig. 6(A) and 40% and 75% thickness in Fig. 6(B), may be due to imaging parameters, tissue microstructure, or sample preparation for histology. Future investigations of BTI that employ more detailed histological investigation or advanced optical imaging techniques as validation can reveal detailed characteristics of the performance of BTI that may improve the performance of the imaging technique and aid in translation of BTI as a clinical imaging modality.

An additional hurdle for clinical translation of BTI is its reliance on precise beamforming and assumptions of ideal ultrasound propagation. BTI is sensitive to aberration of transmitted and backscattered ultrasound pulses as demonstrated in our previous work[16] and further illustrated above in Figs. 5(C) and 6(B). While the rapid variation of microstructure in the epicardial layer is unique to the porcine RV[21] and not observed in human RV tissues,[7] several other sources of aberration are present *in vivo* such as layers of skin, muscle, and fat.

Due to the rotational ultrasound scan, tissue strain calculation with 3DUST is subject to heterogeneous spatial resolution in which the speckle size increases with distance from the axis of rotation in the plane perpendicular to the imaging axis. Speckle coherence is thus reduced more than a few millimeters from the imaging axis, somewhat restricting the field of view of the 3DUST calculation (approximately 6 × 6 mm) compared to the optical camera field of view (approximately 8 × 10 mm). Some error may be introduced to the 3DUST calculation due to misalignment of the rotation and imaging axes as well, although that was found insignificant in the present study such that 3DUST produced accurate and high fidelity measures of tissue deformation near the imaging axis. Additionally, the time-consuming rotational scan required mechanical testing to be performed quasi-statically with careful consideration of viscoelastic effects. Thus the loading protocols were based on our previous studies of 3DUST in BMT, and viscoelasticity was found to not influence the measurement.[8] However, the need for several preconditioning cycles to the largest stretch introduced irreversible tissue damage prior to the measurement cycles of the protocol. Future studies may instead implement a loading protocol similar to that of Sommer et al.,[7] where preconditioning occurs at each stretch level prior to a single measurement cycle, thereby avoiding tissue damage until reaching the cycles with largest applied stretch.

Many of the limitations identified above may be overcome by performing the BTI and 3DUST measurements with a fully populated 2D matrix imaging array. The total information obtained during the 79 s long rotational scan, including direction dependence

of the spatial coherence and 3D B mode imaging for 3DUST, may be obtained in a few milliseconds during a single acquisition using a matrix array. Thus potential errors from misalignment of the rotational axis, heterogeneity of the 3D B mode resolution, and the need for quasi-static mechanical testing may be avoided through use of a matrix array. Unfortunately, such arrays at the frequency employed in this study (18 MHz) are not yet widely available. Once available, fabrication of singular device incorporating 3D volume ultrasound imaging with a matrix array will improve the experimental configuration, as well as open the door for studies of tissue viscoelastic properties, which are the subject of recent biomechanical and clinical interest,[7,25] with dynamic rate-controlled BMT experimentation.

An important limitation to acknowledge with respect to biaxial testing is the neglect of ventricular curvature during biaxial testing. In the present study, as in others, passive deformation in diastole *in vivo* is only approximated in biaxial testing. Planar samples are excised from the ellipsoidal ventricle, and planar deformation is applied to emulate passive pressure-induced stretch in diastole. Thus kinematic or mechanical effects of ventricular curvature, which are important for *in vivo* applications and *in silico* investigations, are not captured in measurements. The assumption is justified by using thin samples with small thickness compared to both sample width and *in vivo* ventricular curvature. The present BMT study employed the thickest samples to date, to the authors' knowledge, yet still with small thickness compared to sample width (~25%) and ventricular curvature (~15%).[26] More complete characterization of myocardium mechanical properties can be obtained using a multifaceted approach similar to that of Sommer et al.,[7] in which planar samples were tested from various locations in free wall thickness ranging from subepicardial to subendocardial, although effects from residual stresses or interactions between layers and are not captured in that approach.

Future directions will aim to leverage the advantages of simultaneous structural and mechanical measurement during biaxial testing, and also overcome the limitations discussed above. Biaxial testing measurements are typically coupled to a constitutive tissue model in order to evaluate the inverse problem and ultimately draw quantitative conclusions about the tissue mechanics. Fiber orientation and tissue strain estimation with ultrasound provide more complete data for evaluation of the inverse problem than the current standard of practice for biaxial testing. For example, the simultaneous measurements of tissue microstructure and deformation may be combined with a detailed and multi-scale finite-element tissue model[26] for enhanced evaluation of tissue mechanical properties.

Future applications in this direction will use the combined measurement configuration and FEA-based inverse analysis to study human ventricular remodeling in chronic heart diseases like pulmonary hypertension (PH), where both mechanical and structural remodeling are tied to disease progress and patient outcomes.[4,27] Demonstration of the new technique on both left and right ventricular tissues was carried out in the present study as PH is commonly associated with left-heart disease, but the end pathway is usually RV failure.[28] Measurement of 3D tissue deformation with ultrasound allows for testing of samples of greater thickness than previous BMT studies of human myocardium,[7] including up to half-thickness LV free wall tissues and fullthickness RV tissues, which are typically around 13–15 mm and 3–5 mm in thickness, respectively.

Acknowledgments

This work was supported by NIH grant Nos. R01AG058659, F32HL160051, and T32HL129964.

Data Availability

All data used in this study are available upon reasonable request from the authors.

References

[1]. Streeter DD and Bassett DL. An engineering analysis of myocardial fiber orientation in pig's left ventricle in systole. Anat. Rec 1966;155:503–512.

[2]. Hooks DA, Trew ML, Caldwell BJ, Sands GB, LeGrice IJ, and Smaill BH. Laminar arrangement of ventricular myocytes influences electrical behavior of the heart. Circ. Res 2007;101:e103–e112. [PubMed: 17947797]

[3]. Chen J, Song S-K, Liu W, McLean M, Allen JS, Tan J, Wickline SA, and Yu X. Remodeling of cardiac fiber structure after infarction in rats quantified with diffusion tensor MRI. Am. J. Physiol. Heart Circ. Physiol 2003;285:H946–H954. [PubMed: 12763752]

[4]. Hill MR, Simon MA, Valdez-Jasso D, Zhang W, Champion HC, and Sacks MS. Structural and mechanical adaptations of right ventricle free wall myocardium to pressure overload. Ann. Biomed. Eng 2014;42:2451–2465. [PubMed: 25164124]

[5]. Sharifi Kia D, Shen Y, Bachman TN, Goncharova EA, Kim K, and Simon MA. The effects of healthy aging on right ventricular structure and biomechanical properties: A pilot study. Front. Med 2022;8:751338.

[6]. Sharifi Kia D, Benza E, Bachman TN, Tushak C, Kim K, and Simon MA. Angiotensin receptor-neprilysin inhibition attenuates right ventricular remodeling in pulmonary hypertension. J. Am. Heart. Assoc 2020;9:e015708. [PubMed: 32552157]

[7]. Sommer G, Schriefl AJ, Andrä M, Sacherer M, Viertler C, Wolinski H, and Holzapfel GA. Biomechanical properties and microstructure of human ventricular myocardium. Acta Biomat 2015;24:172–192.

[8]. Yap CH, Park DW, Dutta D, Simon M, and Kim K. Methods for using 3-D ultrasound speckle tracking in biaxial mechanical testing of biological tissue samples. Ultrasound in Med. Biol 2015;41:1029–1042. [PubMed: 25616585]

[9]. Park DW, Sebastiani A, Yap CH, Simon MA, and Kim K. Quantification of coupled stiffness and fiber orientation remodeling in hypertensive rat right-ventricular myocardium using 3D ultrasound speckle tracking with biaxial testing. PLoS ONE 2016;11:e1065320.

[10]. Papadacci C, Tanter M, Pernot M, and Fink M. Ultrasound backscatter tensor imaging (BTI): Analysis of the spatial coherence of ultrasonic speckle in anisotropic tissues. IEEE Trans. Ult. Ferr. and Freq. Cont 2014;61:968–996.

[11]. Derode A and Fink M. Partial coherence of transient ultrasonic fields in anisotropic random media: Application to coherent echo detection. J. Acoust. Soc. Am 1997;101:690–704.

[12]. Papadacci C, Finel V, Provost J, Villemain O, Bruneval P, Gennisson J-L, Tanter M, Fink M, and Pernot M, "Imaging the dynamics of cardiac fiber orientation in vivo using 3D ultrasound backscatter tensor imaging. Sci. Rep 2017;7:830. [PubMed: 28400606]

[13]. Fixsen LS and Lopata RGP. Ultrasound-based estimation of fibre-directional strain: a simulation study. Ultrasound Med. Biol2022;48:1785–1796. [PubMed: 35764454]

[14]. Sacks MS. A method for planar biaxial mechanical testing that includes in-plane shear. J. Biomech. Eng 1999;121:551–555. [PubMed: 10529924]

[15]. Sommer G, Haspinger DCh, Andrä M, Sacherer M, Viertler C, Regitnig P, and Holzapfel GA. Quantification of shear deformations and corresponding stresses in the biaxially tested human myocardium. Annals of Biomed. Eng 2015;43:2334–2348.

[16]. Cormack JM, Simon MA, and Kim K. Refraction-corrected backscatter tensor imaging of excised porcine ventricular myocardium. JASA Express Lett 2022;2:092001. [PubMed: 36182344]

[17]. Mallart R and Fink M. Adaptive focusing in scattering media through sound-speed inhomogeneities: The van Cittert Zernike approach and focusing criterion. J. Acoust. Soc. Am 1994;96:3721–3732.

[18]. Chen X, Xie H, Kim K, Jia C, Rubin JM, and O'Donnell M. 3-D Correlation-based speckle tracking. Ultrasonic Imaging 2005;27:27–36.

[19]. Püspoki Z, Storath M, Sage D, and Unser M. Transforms and operators for directional bioimage analysis: a survey. Adv. Anat. Embryol. Cell Biol2016;219:69–93. [PubMed: 27207363]

[20]. Ramalli A, Santos P, and D'hooge J. Ultrasound imaging of cardiac fiber orientation: What are we looking at? Proc. IEEE Int Ultrason Symp 2018;1–9.

[21]. Vetter FJ, Simons SB, Mironov S, Hyatt CJ, and Pertsov AM. Epicardial fiber organization in swine right ventricle and its impact on propagation. Circ. Research2005;96:244–251.

[22]. McEnvoy E, Holzapfel GA, and McGarry P. Compressibility and anisotropy of the ventricular myocardium: Experimental analysis and microstructural modeling. J. Biomech. Eng 2018;140:081004.

[23]. Avazmohammadi R, Soares JS, Li DS, Eperjesi T, Pilla J, Gorman RC, and Sacks MS. On the in vivo systolic compressibility of left ventricular free wall myocardium in the normal and infarcted heart. J. Biomech 2020;107:109767. [PubMed: 32386714]

[24]. Nemavhola F Study of biaxial mechanical properties of the passive pig heart: Material characterization and categorization of regional differences. Int. J. Mech. Mater. Eng 2021;16:6 (14 pages).

[25]. Hayabuchi Y, Homma Y, and Kagami S. Right ventricular myocardial stiffness and relaxation components by kinematic model-based transtricuspid flow analysis in children and adolescents with pulmonary arterial hypertension. Ultrasound Med. Biol 2019;45:1999–2009. [PubMed: 31122811]

[26]. Sharifi Kia D, Fortunato R, Maiti S, Simon MA, and Kim K. An exploratory assessment of stretch-induced transmural myocardial fiber kinematics in right ventricular pressure overload. Sci. Rep 2021;11:3587. [PubMed: 33574400]

[27]. Ryo K, Goda A, Onishi T, Delgado-Montero A, Tayal B, Champion HC, Simon MA, Mathier MA, Gladwin MT, and Gorcsan III J. Characterization of right ventricular remodeling in pulmonary hypertension associated with patient outcomes by 3-dimensional wall motion tracking echocardiography. Circ. Cardiovascular Imag 2015;8:e003176.

[28]. Noordegraaf AV, Groeneveldt JA, and Bogaard HJ. Pulmonary hypertension. Eur. Respir. Rev 2016;25:4–11. [PubMed: 26929415]

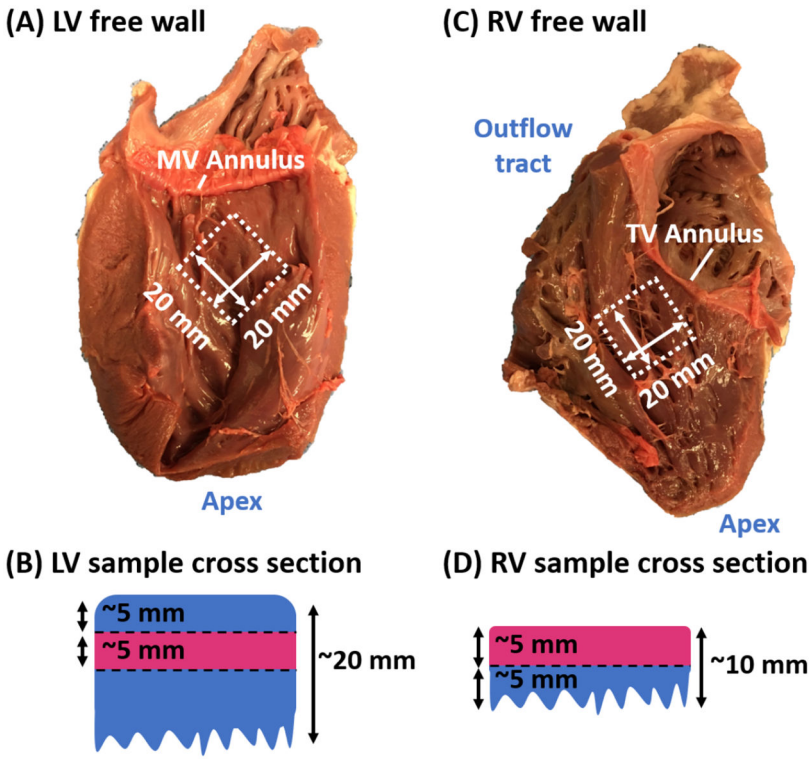

Figure 1:

(A) and (C): Approximate location and orientation of tested excised tissues samples from (A) left ventricle (LV) and (C) right ventricle (RV) free walls, respectively. (B) and (D): Cross sectional views of excised free walls of (B) LV and (D) RV, respectively, illustrating the locations of samples through free wall thickness. Blue and pink correspond to discarded and tested tissues, respectively.

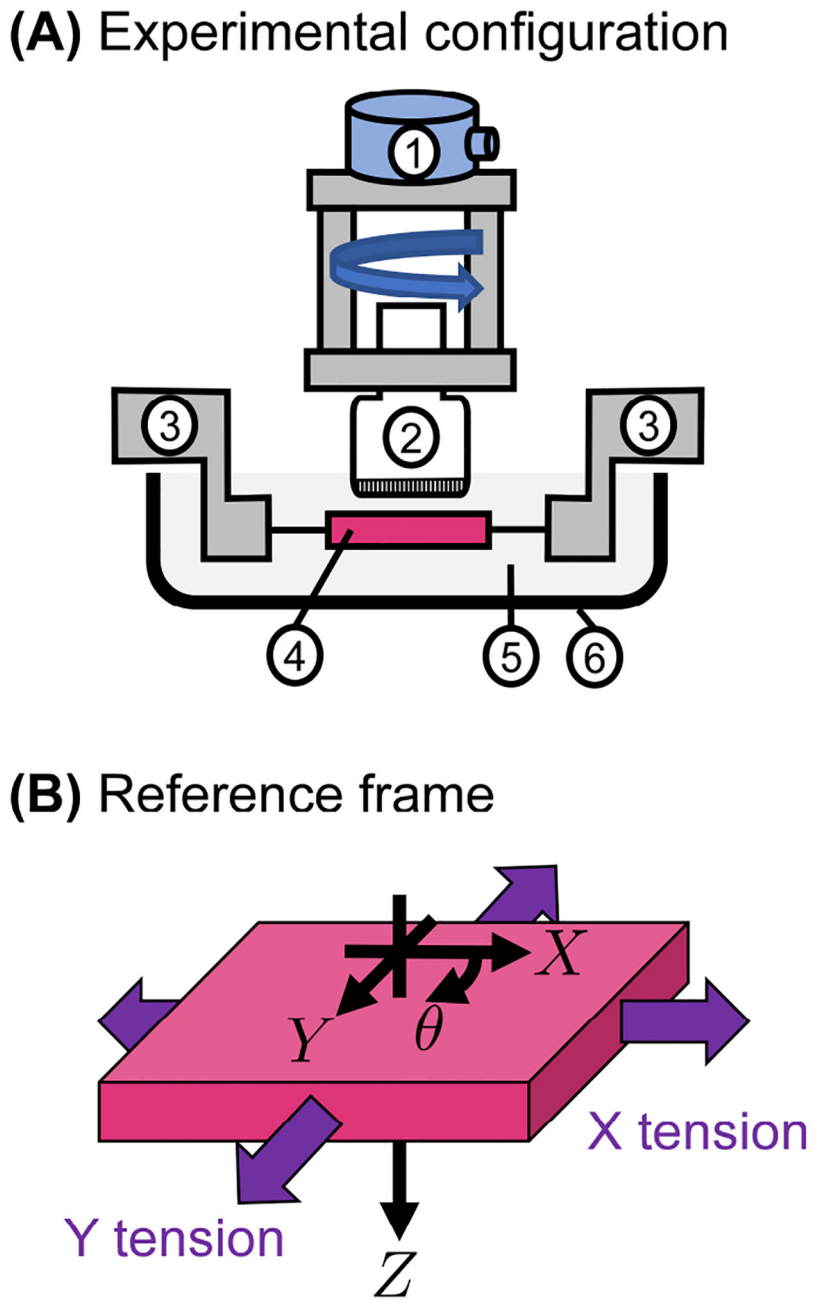

Figure 2:

(A) Schematic illustration of the experimental configuration: (1) Motorized rotational stage, (2) ultrasound imaging array, (3) biaxial testing machine actuators, (4) tissue sample, (5) PBS bath, and (6) fluid tank. (B) Depiction of the reference frame: X and Y directions coincide with directions of BioTester linear actuator motion, Z direction coincides with the ultrasound imaging axis. Angular coordinate θ increases with rotation away from the X axis towards the Y axis: $\theta = \tan^{-1}(Y/X)$. The origin is located at the center of the ultrasound imaging array. Purple arrows indicate tension in the X and Y directions applied by the BioTester.

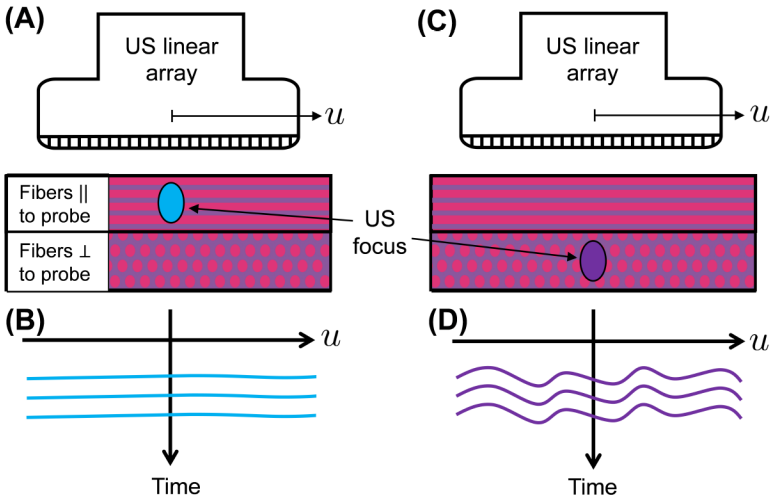

Figure 3:

Operating principle of BTI: (A) When the imaging array direction *u* is aligned with the fiber direction in the focal region, the back scattered wavefronts [blue curves in (B)] exhibit high spatial coherence along the *u* direction. (C) When the fibers are perpendicular to *u* in the focal region, the backscattered wavefronts [purple curves in (D)] exhibit reduced spatial coherence along *u*.

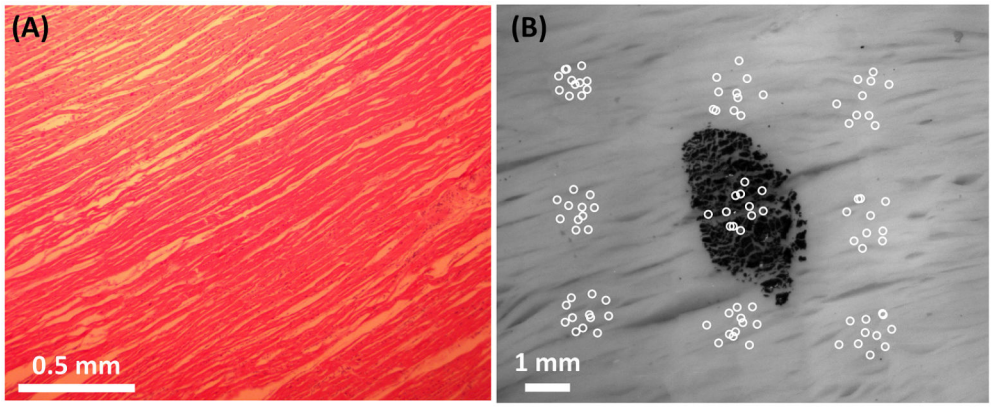

Figure 4:

(A) Histological image of LV tissue following sectioning and staining with H&E. (B) CCD camera image of the tissue surface in the reference configuration. White circles in (B) are the locations of virtual tracking markers used to compute surface strains. The ink pen dot in (B) is used to spatially align the camera and ultrasound measurements.

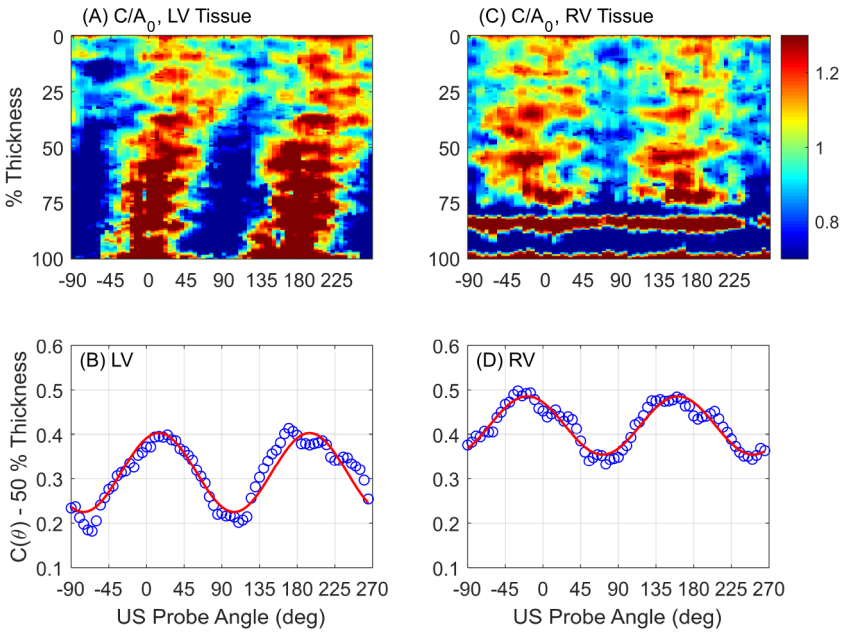

Figure 5:

(A) and (C): Normalized spatial coherence versus ultrasound probe angle and depth through the tissue thickness for an LV and RV sample, respectively. (B) and (D): Measured spatial coherence (blue circles) and cosine fit (red curve) at 50% thickness corresponding to (A) and (C), respectively.

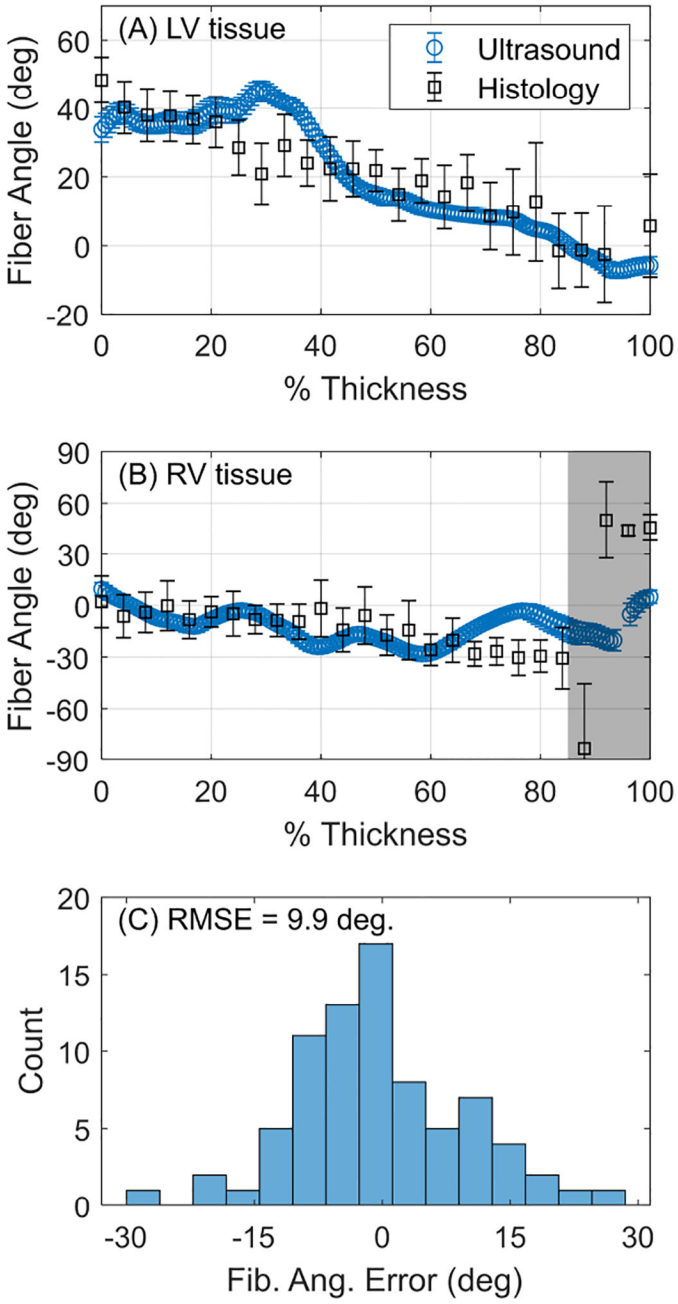

Figure 6:

(A) and (B): Fiber angle predicted by ultrasound (blue circles) and histology (ground truth, black squares) for the LV and RV samples shown in Fig. 5. Error bars for ultrasound represent uncertainty in the fit of Eq. (2) and for histology represent pixel orientation dispersion. The grey area in (B) corresponds to the epicardial region of the RV characterized by rapid variation in the microstructure. (C) Histogram of error across all four tested samples, defined as the difference between fiber angle predicted by ultrasound and histology. The root-meansquare error (RMSE) is 9.9°.

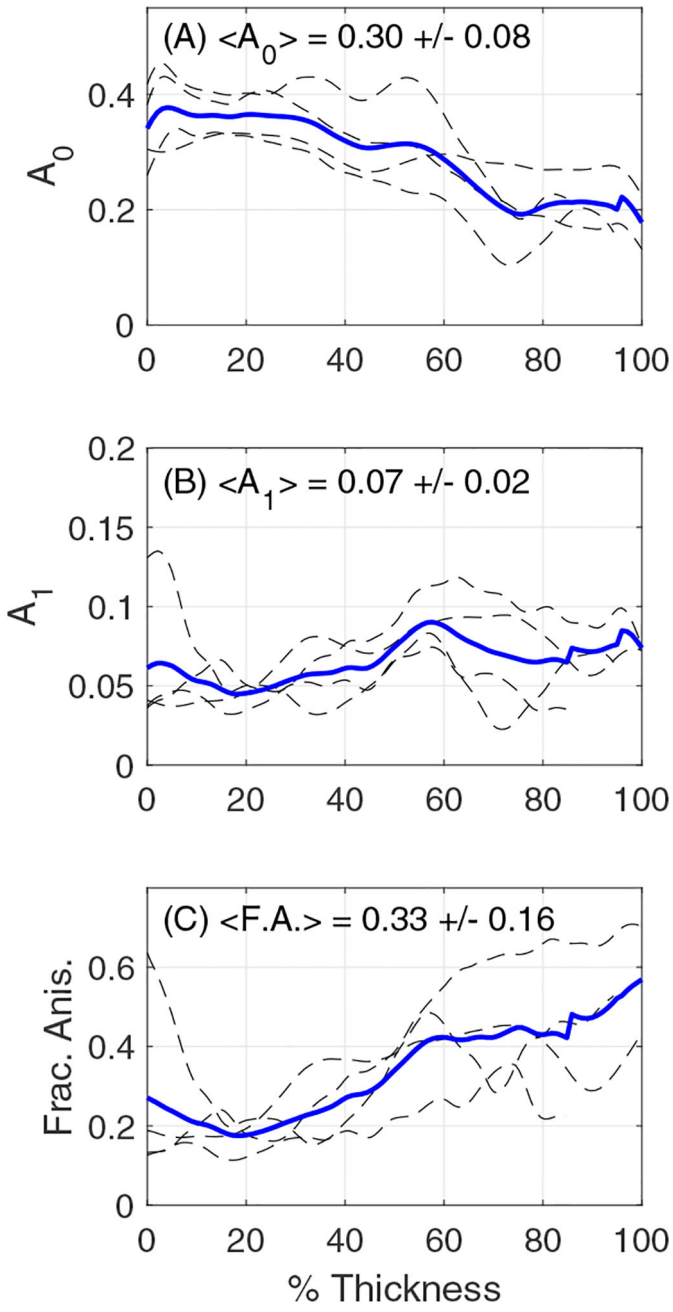

Figure 7:

Transmural and inter-sample variation of (A) mean coherence A_0, (B) coherence modulation A_1, and (C) fractional anisotropy of coherence. Black dashed curves represent metrics for individual samples, and blue solid curves represent the mean. Overall mean $\langle \cdot \rangle$ and standard deviation are presented in each panel. The epicardial layers of the RV samples are not included in these data.

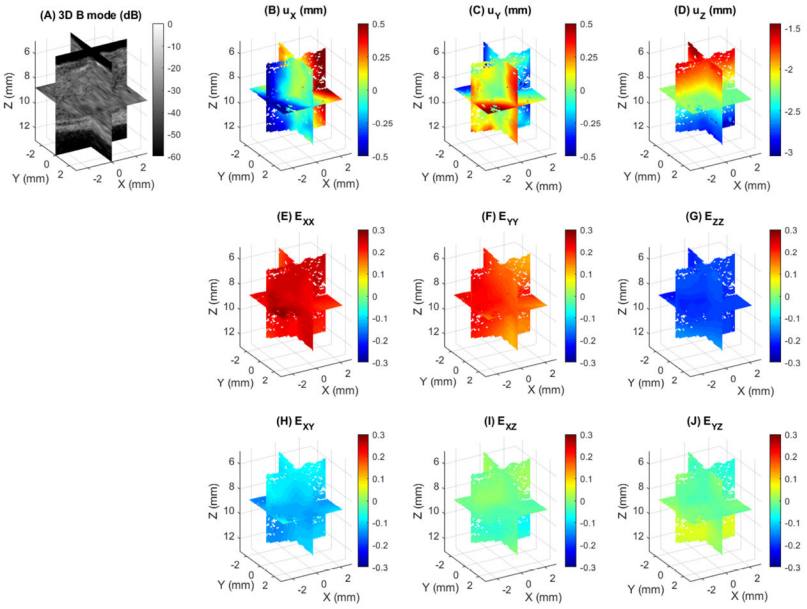

Figure 8:

Tri-plane representations of (A) Ultrasound 3D B mode image of an RV myocardium sample, (B)–(D) displacement components determined using 3DUST and interpolation, (E)–(G), normal strain components, and (H)–(J) shear strain components corresponding to loading condition #1 [approximately equibiaxial, Fig. 9(a)]. The epicardial layer is visible in the B mode image at approximately Z = 11 mm depth.

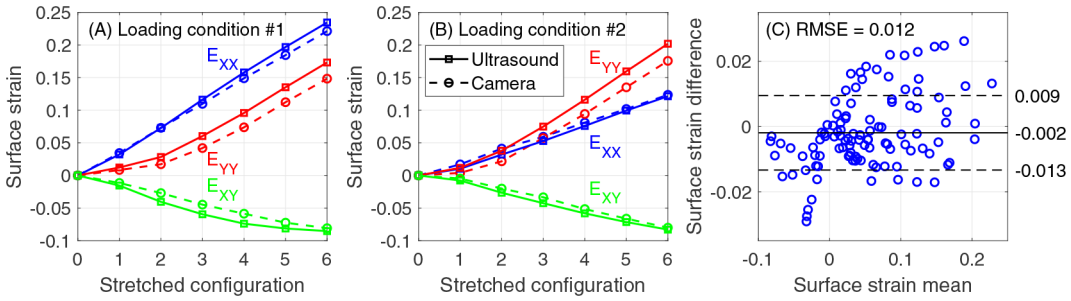

Figure 9:

Validation of ultrasound strain measurement. Surface strains (blue: E_{XX}, red: E_{YY}, green: E_{XY}) obtained from 3DUST and camera imaging (ground truth) for (A) loading condition #1 and (B) loading condition #2. (C) Bland-Altman plot of all surface strain measurements; solid and dashed horizontal lines represent the mean error and +/− one standard deviation. RMSE is 0.012.

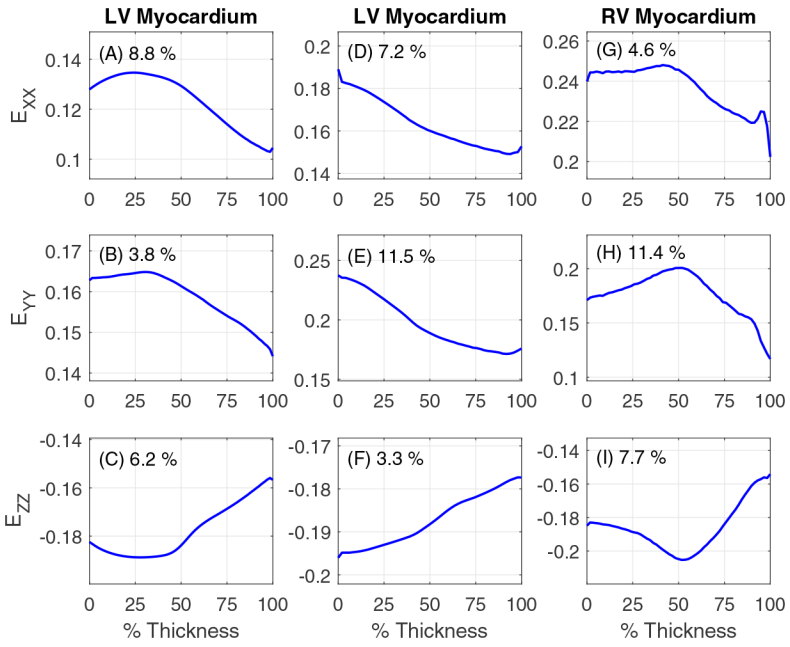

Figure 10:

Variation of normal strain components (rows) of each sample (columns) through the tissue sample thickness (0% and 100% correspond to tissue surfaces near to the array and far from the array, respectively). Transmural percent variation (standard deviation normalized by mean) is presented for each panel. Overall transmural variation is 7.2 ± 3.0%.

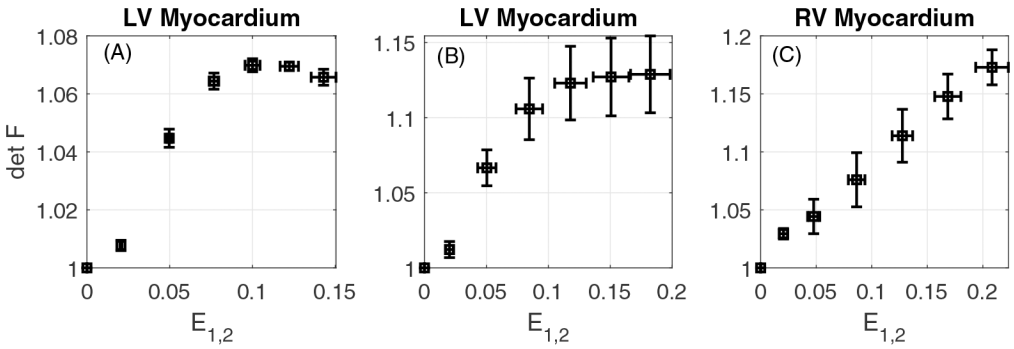

Figure 11:

Tissue volume change det **F** versus mean principle tensile strain $E_{1,2}$ (mean of positive eigenvalues of **E**) for each sample. Error bars indicate transmural variation of each field.

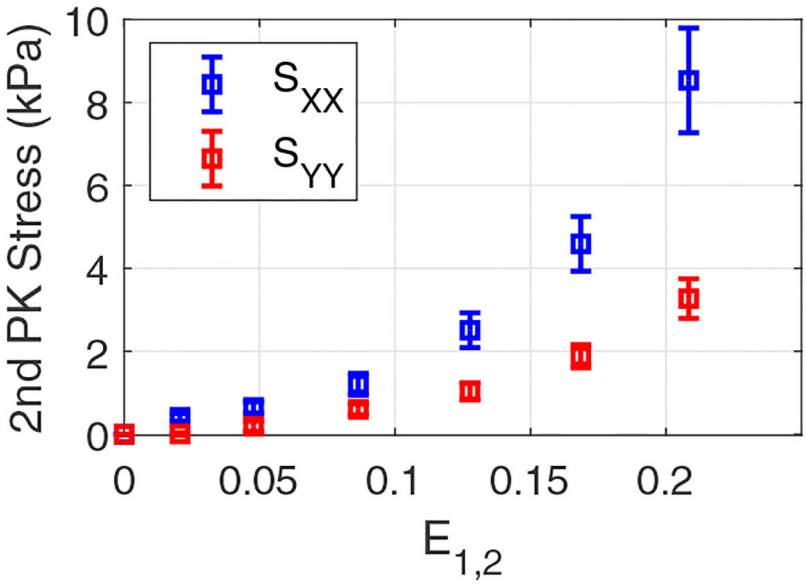

Figure 12:

Stress versus strain corresponding to loading protocol #1 (approximately equibiaxial) for an RV myocardium sample. Blue and red data points are normal stress in the X and Y directions, respectively, at the end of the stretching phase of each loading cycle. Data points and error bars are the mean and standard deviation within a 2 second window (10 samples) around the end of each stretch phase.